Nonresonant Broadband Funneling of Light via Ultrasubwavelength Channels

G. Subramania,[1,3,*] S. Foteinopoulou,[2] and I. Brener[1,4]

[1]*Sandia National Laboratories, P.O. Box 5800, Albuquerque, New Mexico 87185, USA*
[2]*School of Physics, CEMPS, University of Exeter, Exeter EX4 4QL, United Kingdom*
[3]*Department of Electrical and Computer Engineering, University of New Mexico, Albuquerque, New Mexico 87131, USA*
[4]*Center for Integrated Nanotechnologies, Sandia National Laboratories, P.O. Box 5800, Albuquerque, New Mexico 87185, USA*

(Received 28 April 2011; revised manuscript received 28 June 2011; published 13 October 2011)

Enhancing and funneling light efficiently through deep subwavelength apertures is essential in harnessing light-matter interaction. Thus far, this has been accomplished resonantly, by exciting the structural surface plasmons of perforated nanostructured metal films, a phenomenon known as extraordinary optical transmission. Here, we present a new paradigm structure which possesses all the capabilities of extraordinary optical transmission platforms, yet operates nonresonantly on a distinctly different mechanism. Our proposed platform demonstrates efficient ultrabroadband funneling of optical power confined in an area as small as $\sim(\frac{\lambda}{500})^2$, where optical fields are enhanced, thus exhibiting functional possibilities beyond resonant platforms. We analyze the nonresonant mechanism underpinning such a phenomenon with a simple quasistatic picture, which shows excellent agreement with our numerical simulations.

DOI: 10.1103/PhysRevLett.107.163902 PACS numbers: 42.25.−p, 41.20.Jb, 78.20.Ci, 78.67.−n

Confining and enhancing light within deep subwavelength volumes is key to the enhancement of light-matter interaction, with great implications in the control of absorption and emission rates, as well as in attaining high optical nonlinearities and/or gain. However, certain applications also crucially require efficient power funneling of the confined and enhanced electromagnetic fields. Such a phenomenon was demonstrated for the first time in a thin silver film patterned with subwavelength-sized cylindrical holes [1]. In that work, the transmitted light is beyond the expectations of Bethe's theory [2,3] and twice the amount predicted from a simple analysis based on the area fraction of the holes. Therefore, such a phenomenon was termed as an extraordinary optical transmission (EOT). An important goal has been towards optimization of the pertinent features of the phenomenon [4]: field confinement and enhancement, and power throughput exceeding the area fraction of the holes. It is now widely accepted that the EOT phenomenon is a resonant phenomenon mediated by surface plasmon excitation [5,6].

Resonant phenomena unavoidably have a narrow spectral bandwidth. There can be some rather limited control of the bandwidth by engineering the interaction between resonances. For example, by exploiting coupled resonances, a broadened bandwidth was observed in the enhancement around nanoparticle dimers [7] or in the transmission through a metallic grating [8]. Typically, this type of approach would require fine tuning of the structural features: size [7,8], shape [9–12], and/or angle of wave incidence [8]. It is therefore of utmost interest to explore the possibility to access the attractive features of the EOT phenomenon, pertinent to practical applications, but without invoking any resonances. Very recently, Alu *et al.* [13] reported a nonresonant approach to a broadband transmission of P-polarized light through a metallic grating structure, occurring at the Brewster angle of the corresponding effective medium. Nevertheless, such a platform does not offer a two-dimensional confinement of the optical fields and leads to poor field enhancement due to the reduced tangential electric field component [13]. Moreover, the required oblique incidence at large angles can be considerably less practical.

In this Letter, we explore highly efficient funneling of light enhanced in intensity through deep subwavelength apertures facilitated by means of a nonresonant mechanism. We propose a paradigm structure which comprises periodic connected rectangular apertures of two different sizes operating under normal incidence. The larger aperture aids the coupling of the incoming light, while a significant fraction of the incident power is funneled through the smaller aperture. The nonresonant operation renders the proposed structure functional in a very broad wavelength range, starting from 3 μm and continuing well into far-IR wavelengths. The mid-IR wavelength range is of particular interest for molecular fingerprinting or sensing [14], as well as detectors [15]. The broadband functionality allows for flexible utilization in many applications, thus considerably relaxing the stringent design requirements of resonant devices. We will demonstrate in the following how our proposed structure functions as a broadband nonresonant platform that funnels power through a region as small as $(\sim\lambda/500)^2$ (at a 20 μm wavelength) accompanied by highly enhanced electromagnetic fields.

The proposed structure is a square lattice of period a, consisting of alternating small and large rectangular slits engraved on a thin Au film of thickness d_{Au} resting on top a substrate of refractive index of $n = 1.45$ and thickness d_{sub} (Fig. 1). The dimensions of the large and small slits are

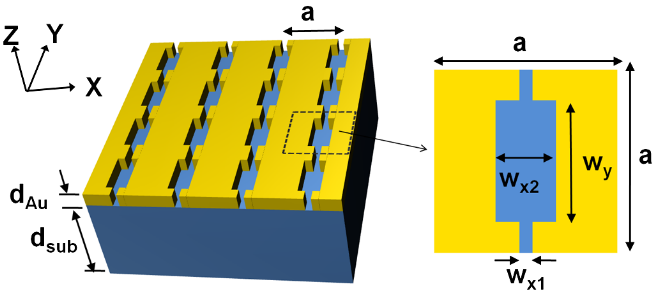

FIG. 1 (color online). The proposed paradigm structure consists of Au patterned film of thickness d_{Au} resting on a d_{sub} thick substrate. The unit cell of the underlying square lattice is magnified and depicted on the right panel (top view), with the associated geometric features designated.

shown in the right panel of Fig. 1. In the limit of $w_{x1} = 0$, we obtain a rectangular-hole structure. When $w_{x1} = w_{x2}$, we obtain a wire-grid (WG) structure, which is widely used as a polarizer due to the polarization selective broadband transparency properties [16]. In the following, we will refer to our proposed structure, where neither $w_{x1} = w_{x2}$ nor $w_{x1} = 0$, as the double-groove (DG) structure.

To understand and explore the optical capabilities of the DG structure, we study numerically the corresponding transmission spectrum between the wavelength range of 3–20 μm. We employ the finite difference time domain (FDTD) approach [17], alongside with the auxiliary differential equation [7,17] method suitable for the modeling of the Drude dispersion [18] for the permittivity [$\varepsilon(\omega)$] in the time domain [7]. For comparison, we consider five different structures (two DG structures, two WG structures, and one rectangular-hole structure). All are chosen to be deeply subwavelength to target the widest operation wavelength regime in the mid-IR while being realistically achievable with nanofabrication methods [19].

We show the simulation results for the transmission in Fig. 2 versus the free space wavelength, $\lambda_{\rm free}$, for a plane wave impinging the structure normally along the z direction, with the electric field polarized along the x direction. All the considered structures have the following feature-size parameters in common: $a = 300$ nm, $d_{Au} = 50$ nm, $d_{sub} = 500$ nm, and $w_y = 200$ nm. We observe a very low transmission for the rectangular structure ($w_{x1} = 0$ nm and $w_{x2} = 100$ nm), represented with the dot-dashed line in Fig. 2. This is expected for a structure comprised of closed shaped apertures for wavelengths above the EOT resonance [2,3]. On the other hand, all structures with unbounded apertures are highly transmissive. In particular, both DG structures—with $(w_{x1}, w_{x2}) = (15\text{ nm}, 100\text{ nm})$ and $(w_{x1}, w_{x2}) = (50\text{ nm}, 100\text{ nm})$, respectively—remain highly transmissive throughout the 3–20 μm range. The corresponding transmission (solid and dashed lines in Fig. 2) lies between that of the 100 nm WG (dotted line) and the 15 nm WG (long-dashed line). The transmission drops sharply around ~3 μm when the incoming fields start to sense the spatial periodicity of the structures [20]. Interestingly, the reduction in total transmission, in reference to the 100 nm WG transmission, is disproportionate with respect to the reduction in w_{x1}, with $w_{x1} = 50$ nm showing negligible change and $w_{x1} = 15$ nm showing a maximum reduction of ~20%.

To understand this behavior, we calculate the spatial distributions [21] (Fig. 3) of the modal electric field (magnitude of the x component) normalized to the incident electric field at a wavelength of 10 μm for the cases depicted in Fig. 2. We observe small field values for the rectangular-hole structure (not shown in Fig. 3). For the DG structures [Figs. 3(a) and 3(b)], we observe a highly enhanced field in the small-gap region—which is higher the narrower the small-gap slit—and a small field in the

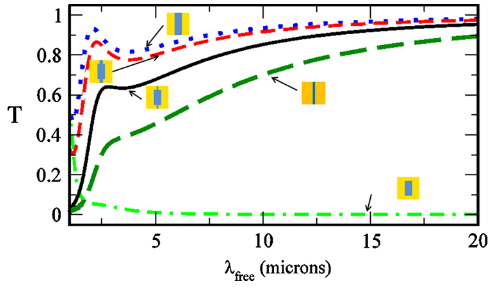

FIG. 2 (color online). Transmission (T) versus free space wavelength in microns. Five variations of the structure depicted in Fig. 1 are considered, all having $d_{Au} = 50$ nm, $d_{sub} = 500$ nm, and $w_y = 200$ nm. (w_{x1} and w_{x2} for each case are given in the text. The adjacent icons depict the corresponding unit cell features to scale.)

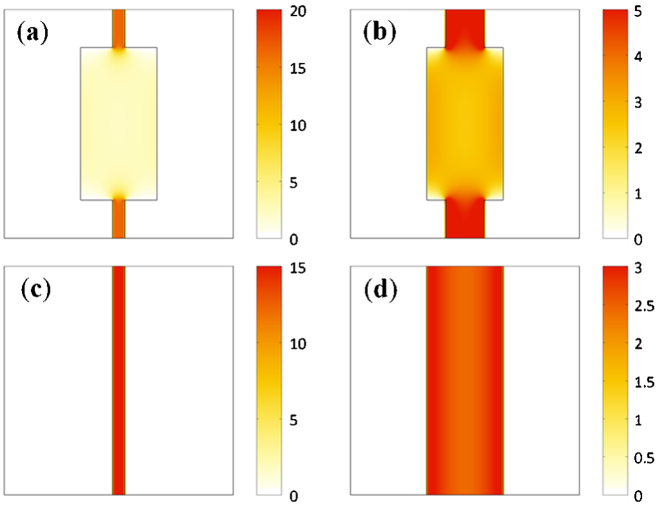

FIG. 3 (color online). Spatial field distribution of the electric field amplitude, normalized to an input field of 1 V/m, at the middle of the Au film [26] for the structures with (a) $w_{x1} = 15$ nm, $w_{x2} = 100$ nm; (b) $w_{x1} = 50$ nm, $w_{x2} = 100$ nm; (c) $w_{x1} = w_{x2} = 15$ nm; and (d) $w_{x1} = w_{x2} = 100$ nm. The remaining structural parameters are as in Fig. 2.

large-gap region. Also, the electric fields remain nearly uniform in the small- and large-slit regions, except for a small fringing at the sharp interface between the two slits. The two WG structures, representing the extreme cases for Figs. 3(a) and 3(b) with $w_{x2} \rightarrow w_{x1} = 15$ nm and $w_{x1} \rightarrow w_{x2} = 100$ nm, respectively, show lower field enhancement values. Strikingly, for both the DG structures, a closer examination of the ratio of the x component of the electric field in the middle of the small and large slit reveals it to be very close to the ratio w_{x2}/w_{x1}.

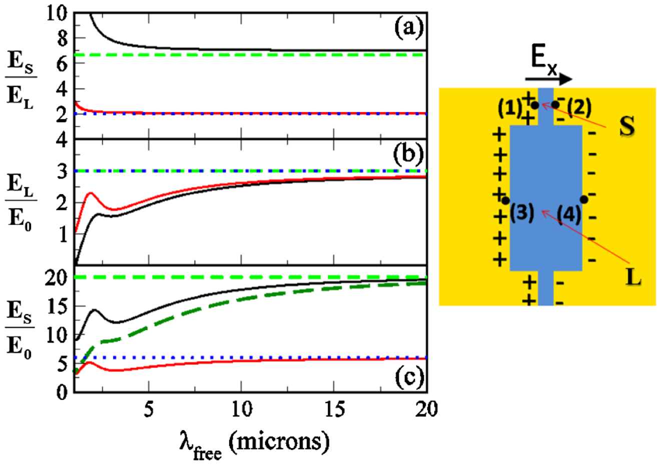

FIG. 4 (color online). Plotted versus free space wavelength: (a) ratio of the electric field amplitudes in the small and large slits; (b) normalized electric field amplitude in the large slit with respect to source amplitude; and (c) normalized electric field amplitude in the small slit with respect to source amplitude. The dark (light) solid lines represent the result for the double-groove structure of Fig. 3(a) [Fig. 3(b)]. For comparison, the result for the 15 nm WG is shown in (c) with a long-dashed line. The dashed (dotted) lines represent the expected result from a quasistatic analysis in the long-wavelength limit for the DG structures of Fig. 3(a) [Fig. 3(b)]. The schematic on the right depicts a simple quasistatic picture of the charge response. The monitoring points are taken at the middle of the Au film. Their locations with respect to the structural unit cell, for the E_S and E_L fields, are also indicated.

Therefore, we further examine this ratio throughout the spectrum of interest (3–20 μm) for the DG structures of Figs. 3(a) and 3(b) and show our results in Fig. 4(a). We observe that, indeed, within this wavelength regime, $E_S/E_L \approxeq w_{x2}/w_{x1}$, with E_S and E_L being the electric field amplitude in the center of the small and large slits, respectively. This can be explained with a simple quasistatic picture, wherein the electrons in the metal respond nearly instantaneously to the incident field. The charges build up across the gaps as depicted in the schematics (right panel of Fig. 4). As a result, the potential difference across the small slit [points (1) and (2)] is equal to the potential difference across the large slit [points (3) and (4)]. This implies a uniform electric field in each respective slit region with no phase difference and an amplitude ratio equal to the inverse of the ratio of the respective widths, as we have observed. In the long-wavelength regime, we can assume the structures are nearly transparent (i.e., almost zero reflection). We apply the continuity of the tangential component of the electric field at the interface [22], but averaged over the structural unit cell, and obtain

$$\frac{E_L w_{x2} w_y + E_S w_{x1}(a - w_y)}{a^2} \approxeq E_0, \qquad (1)$$

with E_0 being the source amplitude. Using in conjunction the quasistatic condition for the E_S/E_L ratio, we get

$$\frac{E_L}{E_0} \approxeq \frac{a}{w_{x2}}, \qquad (2a)$$

$$\frac{E_S}{E_0} \approxeq \frac{a}{w_{x1}}. \qquad (2b)$$

We notice that this simple long-wavelength picture predicts the ratios E_L/E_0 [Fig. 4(b)] and E_S/E_0 [Fig. 4(c)] very well for both considered DG structures down to the 10 μm wavelength, below which it starts to deviate, nevertheless remaining a reasonable estimate down to 3 μm. This is not surprising, as the assumption of near-transparency is not valid as we go towards shorter wavelengths. For the 15 nm WG structure [long-dashed lines in Fig. 4(c)], we find that the deviation from the long-wavelength limit is larger in comparison to the DG structures. Furthermore, we find that the DG structure with $w_{x1} = 15$ nm outperforms the WG structure both in terms of achieved electric field enhancement and in terms of transmission. It is important to note, as we see in Fig. 3, that we have a two-dimensional (2D) confinement of the enhanced optical field for the DG structures, a useful feature for controlling light-matter interaction. This is not the case for the WG structures.

It is of particular interest to evaluate how much power is carried through the small-gap region via the highly confined enhanced electric field. To illustrate this, let us consider the spatial distribution of the z component of the Poynting vector (time-average value), S_z for the DG structure of $w_{x1} = 15$ nm, where we have an electric field enhancement factor of about 20 and confinement of the order of $\sim(\lambda/250)^2$ in the small-slit area at 10 μm [Fig. 5(a)]. As expected, almost no power is transmitted through the metallic region while having a considerably larger power density in the small-slit region compared to the large-slit region.

We calculate the integrated S_z in the small-slit region, P_s, and the large-slit region, P_l, for the DG structure of Fig. 5(a) within the unit cell. The respective areas of integration are designated in Fig. 5. In Fig. 5(b), we show the fraction of power that goes through the small slits, $F_{P_s} = P_s/(P_s + P_l)$, as a function of free space wavelength for such a structure. We observe a large F_{P_s} of about

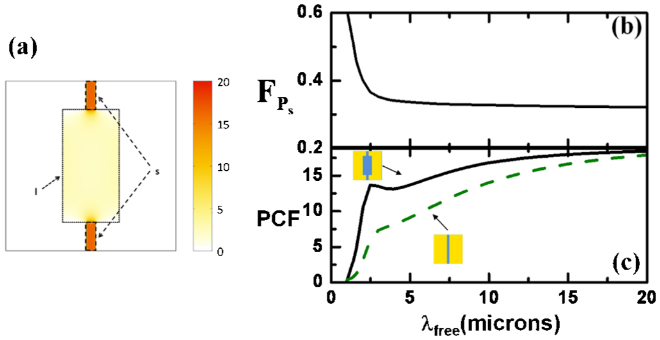

FIG. 5 (color online). (a) Spatial map of the Poynting vector, at the middle of the Au film [27], for the 10 μm incident wavelength for the DG structure of Fig. 3(a) (normalized to the incident Poynting vector). (b) Corresponding ratio of the total power funneled through the small-gap region, F_{P_s}, versus free space wavelength. (c) Comparison of the PCF versus free space wavelength for the DG structure (solid line) of (a) with the 15 nm WG result (dashed line).

30% that remains nearly constant for the entire spectral region of interest [Fig. 5(b)]. This is remarkable, considering that the small-slit region constitutes an area 60 times smaller than the unit cell area. At ~3 μm wavelength, the structural periodicity effects start to emerge, and we observe a sharp increase in F_{P_s} with the total transmission having decreased sharply.

To quantify this behavior, we find it useful to introduce a figure of merit, namely, the "power confinement factor" (PCF). We define PCF as the fraction of the incident power that gets funneled through the small-slit region divided by the area fraction covered by the small-slit region, i.e., $\mathrm{PCF} = TF_{P_s}a^2/A_s$, with A_s being the area covered by the small grooves within the unit cell. It is analogous to the transmission enhancement factor in resonant EOT platforms. To illustrate this, we compare the PCF for the DG structure of Fig. 3(a) to the WG structure of Fig. 3(c) for the same unit cell dimension for consistency, although the WG does not really offer a 2D confinement. The PCFs for both structures are nearly equal (~ 18) at the 20 μm wavelength but decrease at different rates as we approach towards shorter wavelengths, with the PCF for the WG dropping much faster than the one for the DG structure. For example, near the 3 μm wavelength, the PCF for the DG structure is 13.5, while, for the WG, it is about 7.3, nearly half the value.

For this wavelength regime, we observe an almost uniform magnetic field [23]. This enables estimation of the F_{P_s} ratio equaling $1 - w_y/a$ using the quasistatic-limit values for the electric fields [Eqs. (1) and (2)]. Hence, the PCF factor is equal to the field enhancement in the small-slit area [Eq. (2b)], implying that both can be simultaneously optimized. For the parameters of the structure of Fig. 5(a), we obtain $F_{P_s} \sim 33\%$, which is very close to the calculated value of ~30% that we described earlier. When we move away from the long-wavelength limit, the total transmission is better for the structures with the larger air area. The presence of the large aperture enables a more efficient funneling of the enhanced fields through the small aperture. This altogether implies the following: $w_{x2}w_y + w_{x1}(a - w_y)$ controls the total transmission (the higher the greater), w_{x1} controls the enhancement factor of the fields within the slit and PCF factor (the smaller the greater), w_y/a controls the power ratio that goes through the small slits where the field is dramatically enhanced (the smaller the greater), and $w_{x1}(a - w_y)$ controls the 2D confinement (the smaller the better; not applicable for WG). In other words, our proposed platform offers three different independent structural parameters: w_{x2}, w_{x1}, and w_y. By appropriately tuning these parameters, one can control the localization and electric field enhancement, and power confinement, as well as electromagnetic energy transmission through the structure as necessary across a broad wavelength regime, pertinent to application-specific demands.

In conclusion, our results constitute the first counterexample to the widespread and intuitive notion that resonances are needed to funnel light with enhanced intensity through deep subwavelength apertures. We achieve this by employing a simple double-groove structure that effectively combines the broadband transmission property of a one-dimensional grating [16] with the field confinement and enhancement properties of subwavelength apertures. Our structure possesses the attractive features of EOT platforms [4], while being nonresonant and broadband. The structure described is relatively simple to implement and, with constantly improving nanofabrication techniques, is within the realm of possibility in the near future. A higher degree of enhancement is also possible, limited by a lower bound for the small-slit width, imposed by fabrication constraints and the onset of quantum tunneling of charges through the small-slit gap [24]. The demonstrated capabilities of our proposed platform can be important for optofluidic devices [25], enhancement of nonlinear phenomena, and improving absorption efficiency in mid-IR detectors [15].

This work was performed, in part, at the Center for Integrated Nanotechnologies, a U.S. Department of Energy, Office of Basic Energy Sciences user facility. Sandia National Laboratories is a multiprogram laboratory managed and operated by Sandia Corporation, a wholly owned subsidiary of Lockheed Martin Corporation, for the U.S. Department of Energy's National Nuclear Security Administration under Contract No. DE-AC04-94AL85000.

---

[*] Corresponding author.
gssubra@sandia.gov

[1] T. W. Ebbesen, H. J. Lezec, H. F. Ghaemi, T. Thio, and P. A. Wolff, Nature (London) **391**, 667 (1998).
[2] H. A. Bethe, Phys. Rev. **66**, 163 (1944).

[3] C. J. Bouwkamp, Rep. Prog. Phys. **17**, 35 (1954).

[4] C. Genet and E. Ebbesen, Nature (London) **445**, 39 (2007) and references therein.

[5] H. F. Ghaemi, T. Thio, D. E. Grupp, T. W. Ebbesen, and H. J. Lezec, Phys. Rev. B **58**, 6779 (1998).

[6] F. J. Garcia-Vidal, L. Martin-Moreno, T. W. Ebbesen, and L. Kuipers, Rev. Mod. Phys. **82**, 729 (2010).

[7] S. Foteinopoulou, J. P. Vigneron, and C. Vandenbem, Opt. Express **15**, 4253 (2007).

[8] X. R. Huang, R.-W. Peng, and R.-H. Fan, Phys. Rev. Lett. **105**, 243901 (2010).

[9] X. Shi, L. Hesselink, and R. L. Thornton, Opt. Lett. **28**, 1320 (2003).

[10] J. A. Matteo, D. P. Fromm, Y. Yuen, P. J. Schuck, W. E. Moerner, and L. Hesselink, Appl. Phys. Lett. **85**, 648 (2004).

[11] K. Tanaka and M. Tanaka, Opt. Commun. **233**, 231 (2004).

[12] L. Tang, D. A. B. Miller, A. K. Okyay, J. A. Matteo, Y. Yuen, K. C. Saraswat, and L. Hesselink, Opt. Lett. **31**, 1519 (2006).

[13] A. Alu, G. D'Aguanno, N. Mattiucci, and M. J. Bloemer, Phys. Rev. Lett. **106**, 123902 (2011).

[14] C. Yu, A. Ganjoo, H. Jain, C. G. Pantano, and J. Irudayaraj, Anal. Chem. **78**, 2500 (2006).

[15] P. Bhattacharya, A. D. Stiff-Roberts, S. Krishna, and S. Kennerly, International Journal of High Speed Electronics and Systems **12**, 969 (2002).

[16] P. Yeh, Opt. Commun. **26**, 289 (1978).

[17] A. Taflove and S. C. Hagness, *Computational Electrodynamics: The Finite-Difference Time-Domain Method* (Artech House, Boston, 2005), 3rd ed..

[18] $\varepsilon(\omega) = 1.0 - \omega_p^2/[\omega(\omega + i\Gamma)]$, with $\omega_p = 11.78 \times 10^{15}\ \mathrm{rad/sec}$, and $\Gamma = 0.0895 \times 10^{15}\ \mathrm{rad/sec}$. Parameters are determined from an optimal fit to the available data in the region between 1 and 10 μm from E. Palik, *Handbook of Optical Constants of Solids* (Academic, New York, 1985).

[19] J. Henzie, J. Lee, M. H. Lee, W. Hasan, and T. W. Odom, Annu. Rev. Phys. Chem. **60**, 147 (2009).

[20] See Fig. 1 in the Supplemental Material.

[21] This simulation is performed with the Lumerical FDTD Solutions package; Reference Guide for FDTD Solutions Release 7.0.1, http://www.lumerical.com/fdtd.

[22] J. D. Jackson, *Classical Electrodynamics* (Wiley, New York, 1999), 3rd ed..

[23] See Supplemental Material at http://link.aps.org/supplemental/10.1103/PhysRevLett.107.163902 for the magnetic field (y component) at three different wavelengths (Fig. 2).

[24] P. Song, P. Nordlander, and S. W. Gao, J. Chem. Phys. **134**, 074701 (2011).

[25] D. Psaltis, S. R. Quake, and C. H. Yang, Nature (London) **442**, 381 (2006).

[26] The corresponding field map for the structure of Fig. 3(a); however, 20 nm within the substrate is shown in Fig. 3(a) of the Supplemental Material.

[27] The corresponding Poynting vector map; however, 20 nm within the substrate is shown in Fig. 3(b) of the Supplemental Material.